HybridSN: Exploring 3-D–2-D CNN Feature Hierarchy for Hyperspectral Image Classification

Swalpa Kumar Roy, *Student Member, IEEE*, Gopal Krishna, Shiv Ram Dubey , *Member, IEEE*, and Bidyut B. Chaudhuri, *Fellow, IEEE*

Abstract—Hyperspectral image (HSI) classification is widely used for the analysis of remotely sensed images. Hyperspectral imagery includes varying bands of images. Convolutional neural network (CNN) is one of the most frequently used deep learning-based methods for visual data processing. The use of CNN for HSI classification is also visible in recent works. These approaches are mostly based on 2-D CNN. On the other hand, the HSI classification performance is highly dependent on both spatial and spectral information. Very few methods have used the 3-D-CNN because of increased computational complexity. This letter proposes a hybrid spectral CNN (HybridSN) for HSI classification. In general, the HybridSN is a spectral–spatial 3-D-CNN followed by spatial 2-D-CNN. The 3-D-CNN facilitates the joint spatial–spectral feature representation from a stack of spectral bands. The 2-D-CNN on top of the 3-D-CNN further learns more abstract-level spatial representation. Moreover, the use of hybrid CNNs reduces the complexity of the model compared to the use of 3-D-CNN alone. To test the performance of this hybrid approach, very rigorous HSI classification experiments are performed over Indian Pines, University of Pavia, and Salinas Scene remote sensing data sets. The results are compared with the state-of-the-art hand-crafted as well as end-to-end deep learning-based methods. A very satisfactory performance is obtained using the proposed HybridSN for HSI classification. The source code can be found at https://github.com/gokriznastic/HybridSN.

Index Terms—2-D-convolutional neural network (CNN), 3-D-CNN, deep learning, CNNs, hybrid spectral CNN (HybridSN), hyperspectral image (HSI) classification, remote sensing, spectral–spatial.

I. INTRODUCTION

THE research in hyperspectral image (HSI) analysis is important due to its potential applications in real life [1]. Hyperspectral imaging results in multiple bands of images that make the analysis challenging due to the increased volume of data. The spectral, as well as the spatial correlation between different bands, conveys useful information regarding the scene of interest. Recently, Camps-Valls *et al.* [2] have surveyed the advances in HSI classification. The HSI classification is tackled in two ways: one with a hand-designed feature extraction technique and another with learning-based feature extraction technique.

Several HSI classification approaches have been developed using the hand-designed feature description [3], [4]. Yang and Qian [3] have proposed a joint collaborative representation by using the locally adaptive dictionary [3]. It reduces the adverse impact of useless pixels and improves HSI classification performance. Fang *et al.* [4] have utilized the local covariance matrix to encode the relationship between different spectral bands. They used these matrices for HSI training and classification using support vector machine (SVM). A composite kernel is used to combine spatial and spectral information for HSI classification [5]. Li *et al.* [6] have applied the learning over the combination of multiple features for the classification of hyperspectral scenes. Some other hand-crafted approaches are joint sparse model and discontinuity preserving relaxation [7], Boltzmann entropy-based band selection [8], sparse self-representation [9], fusing correlation coefficient and sparse representation [10], multiscale superpixels and guided filter [11], and so on.

Recently, the convolutional neural network (CNN) has become very popular due to its drastic performance gain over the hand-designed features [12]. The CNN has shown very promising performance in many applications where visual information processing is required, such as image classification [13], [14], object detection [15], semantic segmentation [16], colon cancer classification [17], depth estimation [18], and face antispoofing [19]. In recent years, huge progress is also made in deep learning for the HSI analysis. A dual-path network (DPN) by combining the residual network and dense convolutional network is proposed for the HSI classification [20]. Yu *et al.* [21] have proposed a greedy layerwise approach for unsupervised training to represent the remote sensing images. Li *et al.* [22] introduced a pixel-block pair (PBP)-based data augmentation technique to generalize the deep learning for HSI classification [22]. Song *et al.* [23] have proposed a deep feature fusion network and Cheng *et al.* [24] have used the off-the-shelf CNN models for HSI classification. In general, they extracted the hierarchical deep spatial features and used with SVM for training and classification. Recently, the low-power consuming hardware for deep learning-based HSI classification is also explored [25]. Chen *et al.* [26] have used the deep feature extraction of 3-D-CNN for HSI classification. Zhong *et al.* [27] have proposed the spectral–spatial residual network (SSRN). The residual blocks in SSRN use the identity mapping to connect every other 3-D convolutional layer. Mou *et al.* [28] have investigated the residual conv-deconv network, an unsupervised model, for HSI classification. Recently, Paoletti *et al.* [29] have proposed the Deep Pyramidal Residual Networks (DPRN) especially for the
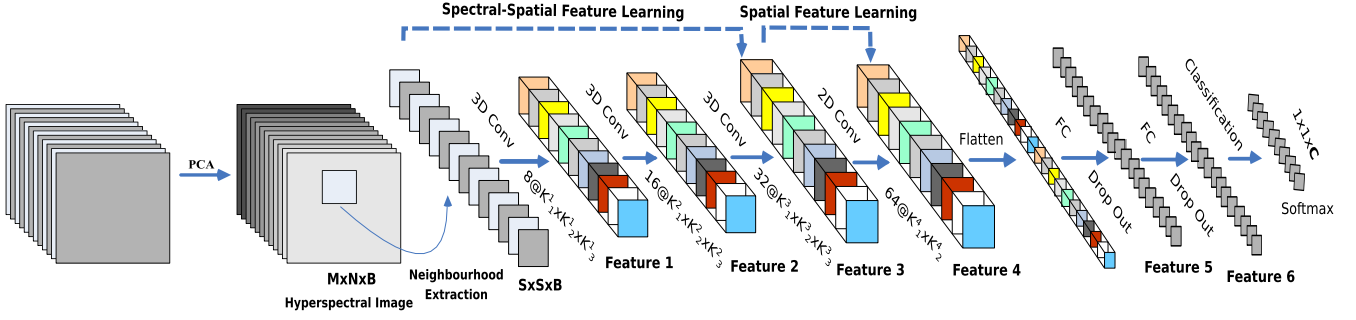
Fig. 1. Proposed HybridSpectralNet (HybridSN) model that integrates 3-D and 2-D convolutions for HSI classification.

HSI data. More recently, Paoletti *et al.* [30] have also proposed spectral–spatial capsule networks to learn the hyperspectral features, whereas Fang *et al.* [31] introduced deep hashing neural networks for HSI feature extraction.

It is evident from the literature that using just 2-D-CNN or 3-D-CNN had a few shortcomings such as missing channel relationship information or very complex model, respectively. It also prevented these methods from achieving better accuracy on HSIs. The main reason is due to the fact that HSIs are volumetric data and have a spectral dimension as well. The 2-D-CNN alone is not able to extract good discriminating feature maps from the spectral dimensions. Similarly, a deep 3-D-CNN is more computationally complex and this alone seems to perform worse for classes having similar textures over many spectral bands. This is the motivation for us to propose a hybrid-CNN model which overcomes these shortcomings of the previous models. The 3-D-CNN and 2-D-CNN layers are assembled for the proposed model in such a way that they utilize both the spectral as well as spatial feature maps to their full extent to achieve maximum possible accuracy.

This letter proposes the hybrid spectral CNN (HybridSN) in Section II; presents the experiments and analysis in Section III; and highlights the concluding remarks in Section IV.

II. PROPOSED HYBRIDSN MODEL

Let the spectral–spatial hyperspectral data cube be denoted by $\mathbf{I} \in \mathcal{R}^{M \times N \times D}$, where $\mathbf{I}$ is the original input, M is the width, N is the height, and D is the number of spectral bands/depth. Every HSI pixel in $\mathbf{I}$ contains D spectral measures and forms a one-hot label vector $Y = (y_1, y_2, \ldots, y_C) \in \mathcal{R}^{1 \times 1 \times C}$, where C represents the land-cover categories. However, the hyperspectral pixels exhibit the mixed land-cover classes, introducing the high intraclass variability and interclass similarity into $\mathbf{I}$. It is of great challenge for any model to tackle this problem. To remove the spectral redundancy first, the traditional principal component analysis (PCA) is applied over the original HSI data ($\mathbf{I}$) along spectral bands. The PCA reduces the number of spectral bands from D to B while maintaining the same spatial dimensions (i.e., width M and height N). We have reduced only spectral bands such that it preserves the spatial information which is very important for recognizing any object. We represent the PCA reduced data cube by $\mathbf{X} \in \mathcal{R}^{M \times N \times B}$, where $\mathbf{X}$ is the modified input after PCA, M is the width, N is the height, and B is the number of spectral bands after PCA.

TABLE I
LAYERWISE SUMMARY OF THE PROPOSED *HYBRIDSN* ARCHITECTURE WITH WINDOW SIZE 25×25. THE LAST LAYER IS BASED ON THE IP DATA SET

Layer (type)	Output Shape	# Parameter
input_1 (InputLayer)	(25, 25, 30, 1)	0
conv3d_1 (Conv3D)	(23, 23, 24, 8)	512
conv3d_2 (Conv3D)	(21, 21, 20, 16)	5776
conv3d_3 (Conv3D)	(19, 19, 18, 32)	13856
reshape_1 (Reshape)	(19, 19, 576)	0
conv2d_1 (Conv2D)	(17, 17, 64)	331840
flatten_1 (Flatten)	(18496)	0
dense_1 (Dense)	(256)	4735232
dropout_1 (Dropout)	(256)	0
dense_2 (Dense)	(128)	32896
dropout_2 (Dropout)	(128)	0
dense_3 (Dense)	(16)	2064

Total Trainable Parameters: 5, 122, 176

In order to utilize the image classification techniques, the HSI data cube is divided into small overlapping 3-D-patches, the truth labels of which are decided by the label of the centered pixel. We have created the 3-D neighboring patches $P \in \mathcal{R}^{S \times S \times B}$ from $\mathbf{X}$, centered at the spatial location (α, β), covering the $S \times S$ window or spatial extent and all B spectral bands. The total number of generated 3-D-patches (n) from X is given by $(M - S + 1) \times (N - S + 1)$. Thus, the 3-D-patch at location (α, β), denoted by $P_{\alpha, \beta}$, covers the width from $\alpha - (S - 1)/2$ to $\alpha + (S - 1)/2$, height from $\beta - (S - 1)/2$ to $\beta + (S - 1)/2$, and all B spectral bands of PCA reduced data cube X.

In 2-D-CNN, the input data are convolved with 2-D kernels. The convolution happens by computing the sum of the dot product between input data and kernel. The kernel is strided over the input data to cover full spatial dimension. The convolved features are passed through the activation function to introduce the nonlinearity in the model. In 2-D convolution, the activation value at spatial position (x, y) in the jth feature map of the ith layer, denoted as $v_{i,j}^{x,y}$, is generated using the following equation:

$$v_{i,j}^{x,y} = \phi \left(b_{i,j} + \sum_{\tau=1}^{d_{l-1}} \sum_{\rho=-\gamma}^{\gamma} \sum_{\sigma=-\delta}^{\delta} w_{i,j,\tau}^{\sigma,\rho} \times v_{i-1,\tau}^{x+\sigma,y+\rho} \right) \quad (1)$$

where ϕ is the activation function, $b_{i,j}$ is the bias parameter for the jth feature map of the ith layer, d_{l-1} is the number of feature map in $(l-1)$th layer and the depth of kernel $w_{i,j}$ for the jth feature map of the ith layer, $2\gamma + 1$ is the width

TABLE II
CLASSIFICATION ACCURACIES (IN PERCENTAGES) ON IP, UP, AND SA DATA SETS USING THE PROPOSED AND STATE-OF-THE-ART METHODS

Methods	Indian Pines Dataset			University of Pavia Dataset			Salinas Scene Dataset		
	OA	Kappa	AA	OA	Kappa	AA	OA	Kappa	AA
SVM	85.30 ± 2.8	83.10 ± 3.2	79.03 ± 2.7	94.34 ± 0.2	92.50 ± 0.7	92.98 ± 0.4	92.95 ± 0.3	92.11 ± 0.2	94.60 ± 2.3
2D-CNN	89.48 ± 0.2	87.96 ± 0.5	86.14 ± 0.8	97.86 ± 0.2	97.16 ± 0.5	96.55 ± 0.0	97.38 ± 0.0	97.08 ± 0.1	98.84 ± 0.1
3D-CNN	91.10 ± 0.4	89.98 ± 0.5	91.58 ± 0.2	96.53 ± 0.1	95.51 ± 0.2	97.57 ± 1.3	93.96 ± 0.2	93.32 ± 0.5	97.01 ± 0.6
M3D-CNN	95.32 ± 0.1	94.70 ± 0.2	96.41 ± 0.7	95.76 ± 0.2	94.50 ± 0.2	95.08 ± 1.2	94.79 ± 0.3	94.20 ± 0.2	96.25 ± 0.6
SSRN	99.19 ± 0.3	99.07 ± 0.3	98.93 ± 0.6	99.90 ± 0.0	99.87 ± 0.0	99.91 ± 0.0	99.98 ± 0.1	99.97 ± 0.1	99.97 ± 0.0
HybridSN	99.75 ± 0.1	99.71 ± 0.1	99.63 ± 0.2	99.98 ± 0.0	99.98 ± 0.0	99.97 ± 0.0	100 ± 0.0	100 ± 0.0	100 ± 0.0

of kernel, $2\delta+1$ is the height of kernel, and $w_{i,j}$ is the value of weight parameter for the jth feature map of the ith layer.

The 3-D convolution [32] is done by convolving a 3-D kernel with the 3-D-data. In the proposed model for HSI data, the feature maps of convolution layer are generated using the 3-D kernel over multiple contiguous bands in the input layer; this captures the spectral information. In 3-D convolution, the activation value at spatial position (x, y, z) in the jth feature map of the ith layer, denoted as $v_{i,j}^{x,y,z}$, is generated as follows:

$$v_{i,j}^{x,y,z}$$
$$= \phi\left(b_{i,j} + \sum_{\tau=1}^{d_{l-1}} \sum_{\lambda=-\eta}^{\eta} \sum_{\rho=-\gamma}^{\gamma} \sum_{\sigma=-\delta}^{\delta} w_{i,j,\tau}^{\sigma,\rho,\lambda} \times v_{i-1,\tau}^{x+\sigma, y+\rho, z+\lambda}\right) \quad (2)$$

where $2\eta + 1$ is the depth of kernel along spectral dimension and other parameters are the same as in (1).

The parameters of CNN, such as the bias b and the kernel weight w, are usually trained using supervised approaches [12] with the help of a gradient descent optimization technique. In conventional 2-D CNNs, the convolutions are applied over the spatial dimensions only, covering all the feature maps of the previous layer, to compute the 2-D discriminative feature maps. On the other hand, for the HSI classification problem, it is desirable to capture the spectral information encoded in multiple bands along with the spatial information. The 2-D-CNNs are not able to handle the spectral information. On the other hand, the 3-D-CNN kernel can extract the spectral and spatial feature representation simultaneously from HSI data but at the cost of increased computational complexity. In order to take the advantages of the automatic feature learning capability of both 2-D and 3-D CNNs, we propose a hybrid feature learning framework called $HybridSN$ for HSI classification. The flow diagram of the proposed $HybridSN$ network is shown in Fig. 1. It comprises three 3-D convolutions (2), one 2-D convolution (1), and three fully connected layers.

In $HybridSN$ framework, the dimensions of 3-D convolution kernels are $8 \times 3 \times 3 \times 7 \times 1$ (i.e., $K_1^1 = 3$, $K_2^1 = 3$, and $K_3^1 = 7$ in Fig. 1), $16 \times 3 \times 3 \times 5 \times 8$ (i.e., $K_1^2 = 3$, $K_2^2 = 3$, and $K_3^2 = 5$ in Fig. 1) and $32 \times 3 \times 3 \times 3 \times 16$ (i.e., $K_1^3 = 3$, $K_2^3 = 3$, and $K_3^3 = 3$ in Fig. 1) in the subsequent first, second, and third convolution layers, respectively, where $16 \times 3 \times 3 \times 5 \times 8$ means 16 3-D-kernels of dimension $3 \times 3 \times 5$ (i.e., two spatial and one spectral dimension) for all eight 3-D input feature maps. On the other hand, the dimension of 2-D convolution kernel is $64 \times 3 \times 3 \times 576$ (i.e., $K_1^4 = 3$ and $K_2^4 = 3$ in Fig. 1), where 64 is the number of 2-D-kernels, 3×3 represents the spatial dimension of 2-D-kernel, and 576

is the number of 2-D input feature maps. To increase the number of spectral–spatial feature maps simultaneously, 3-D convolutions are applied thrice and can preserve the spectral information of input HSI data in the output volume. The 2-D convolution is applied once before the *flatten* layer by keeping in mind that it strongly discriminates the spatial information within different spectral bands without substantial loss of spectral information, which is very important for HSI data. A detailed summary of the proposed model in terms of the layer types, output map dimensions, and number of parameters is given in Table I. It can be seen that the highest number of parameters is present in the first dense layer. The number of node in the last dense layer is 16, which is the same as the number of classes in Indian Pines (IP) data set. Thus, the total number of parameters in the proposed model depends on the number of classes in a data set. The total number of trainable weight parameters in $HybridSN$ is 5, 122, 176 for IP data set. All weights are randomly initialized and trained using back-propagation algorithm with the *Adam* optimizer by using the *softmax* loss. We use mini-batches of size 256 and train the network for 100 epochs with no batch normalization and data augmentation.

III. EXPERIMENTS AND DISCUSSION

A. Data set Description and Training Details

We have used three publicly available HSI data sets,[1] namely, Indian Pines (IP), University of Pavia (UP) and Salinas Scene (SA). The IP data set has images with 145×145 spatial dimension and 224 spectral bands in the wavelength range of 400 to 2500 nm, out of which 24 spectral bands covering the region of water absorption have been discarded. The ground truth available is designated into 16 classes of vegetation. The UP data set consists of 610×340 spatial dimension pixels with 103 spectral bands in the wavelength range of 430–860 nm. The ground truth is divided into nine urban land-cover classes. The SA data set contains the images with 512×217 spatial dimension and 224 spectral bands in the wavelength range of 360–2500 nm. The 20 water absorbing spectral bands have been discarded. In total, 16 classes are present in this data set.

All experiments are conducted on an Acer Predator-Helios laptop with the GTX 1060 graphical processing unit (GPU) and 16 GB RAM. We have chosen the optimal learning rate of 0.001 based on the classification outcomes. In order to make the fair comparison, we have extracted the same spatial dimension in 3-D-patches of input volume for different data

---

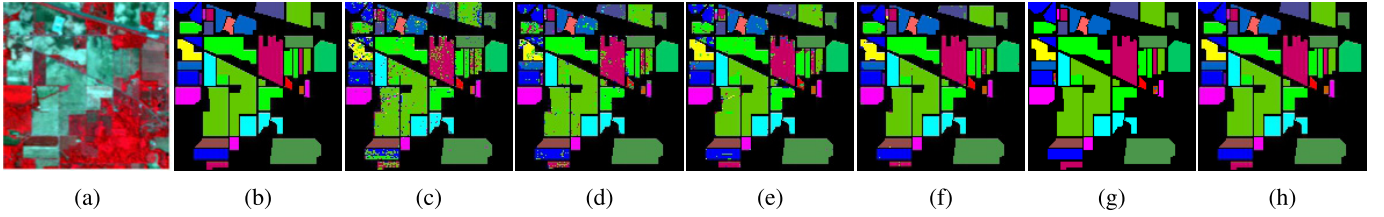[1] www.ehu.eus/ccwintco/index.php/Hyperspectral_Remote_Sensing_Scenes

Fig. 2.   Classification map for IP. (a) False color image. (b) Ground truth. (c)–(h) Predicted classification maps for SVM, 2-D-CNN, 3-D-CNN, M3D-CNN, SSRN, and proposed HybridSN, respectively.
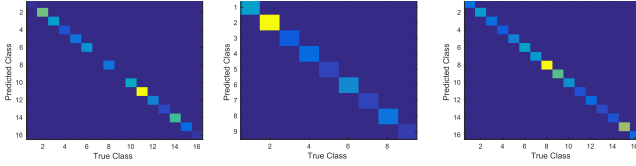

Fig. 3.   Confusion matrix using proposed method over IP, UP, and SA data sets in the first, second, and third matrices, respectively.
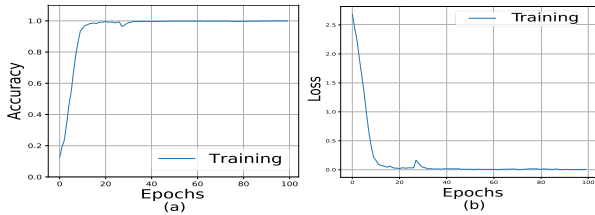

Fig. 4.   Accuracy and loss convergence versus epochs over the IP data set.

sets, such as $25 \times 25 \times 30$ for IP and $25 \times 25 \times 15$ for UP and SA, respectively.

B. Classification Results

In this letter, we have used the overall accuracy (OA), average accuracy (AA), and Kappa coefficient (Kappa) evaluation measures to judge the HSI classification performance. Here, OA represents the number of correctly classified samples out of the total test samples; AA represents the average of classwise classification accuracies; and Kappa is a metric of statistical measurement which provides mutual information regarding a strong agreement between the ground truth map and classification map. The results of the proposed $HybridSN$ model are compared with the most widely used supervised methods, such as SVM [33], 2-D-CNN [34], 3-D-CNN [35], multi-scale 3-D deep convolutional neural network (M3D)-CNN [36], and SSRN [27]. The 30% and 70% of the data are randomly divided into training and testing groups, respectively.[2] We have used the publicly available code[3] of the compared methods to compute the results.

Table II shows the results in terms of the OA, AA, and Kappa for different methods[4] It can be observed from Table II that the $HybridSN$ outperforms all the compared methods over each data set while maintaining the minimum standard deviation. The proposed $HybridSN$ is based on the hierarchical representation of spectral–spatial 3-D-CNN followed by a spatial 2-D-CNN, which are complementary to each other. It is also observed from these results that the performance of 3-D-CNN is poor than 2-D-CNN over SA

[2]More details of data set are provided in the supplementary material.
[3]https://github.com/eecn/Hyperspectral-Classification
[4]The classwise accuracy is provided in the supplementary material.

TABLE III
TRAINING TIME IN MINUTES (m) AND TEST TIME IN SECONDS (s) OVER IP, UP, AND SA DATA SETS USING 2-D-CNN, 3-D-CNN, AND $HybridSN$ ARCHITECTURES

Data	2D CNN		3D CNN		HybridSN	
	Train(m)	Test(s)	Train(m)	Test(s)	Train(m)	Test(s)
IP	1.9	1.1	15.2	4.3	14.1	4.8
UP	1.8	1.3	58.0	10.6	20.3	6.6
SA	2.2	2.0	74	15.2	25.5	9.0

TABLE IV
IMPACT OF THE SPATIAL WINDOW SIZE ON THE PERFORMANCE OF $HybridSN$

Window	IP(%)	UP(%)	SA(%)	Window	IP(%)	UP(%)	SA(%)
19×19	99.74	99.98	99.99	23×23	99.31	99.96	99.71
21×21	99.73	99.90	99.69	25×25	99.75	99.98	100

TABLE V
CLASSIFICATION ACCURACIES (IN PERCENTAGES) USING THE PROPOSED AND STATE-OF-THE-ART METHODS ON LESS AMOUNT OF TRAINING DATA, i.e., 10% ONLY

Methods	Indian Pines			Univ. of Pavia			Salinas Scene		
	OA	Kappa	AA	OA	Kappa	AA	OA	Kappa	AA
2D-CNN	80.27	78.26	68.32	96.63	95.53	94.84	96.34	95.93	94.36
3D-CNN	82.62	79.25	76.51	96.34	94.90	97.03	85.00	83.20	89.63
M3D-CNN	81.39	81.20	75.22	95.95	93.40	97.52	94.20	93.61	96.66
SSRN	98.45	98.23	86.19	99.62	99.50	99.49	99.64	99.60	99.76
HybridSN	98.39	98.16	98.01	99.72	99.64	99.20	99.98	99.98	99.98

data set. To the best of our knowledge, this is probably due to the presence of two classes in the Salinas data set (namely Grapes-untrained and Vinyard-untrained) which have very similar textures over most spectral bands. Hence, due to the increased redundancy among the spectral bands, the 2-D-CNN outperforms the 3-D-CNN over SA data set. Moreover, the performance of SSRN and HybridSN is always far better than M3D-CNN. It is evident that 3-D or 2-D convolution alone is not able to represent the highly discriminative feature compared to hybrid 3-D and 2-D convolutions.

The classification map for an example HSI is shown in Fig. 2 using SVM, 2-D-CNN, 3-D-CNN, M3D-CNN, SSRN, and HybridSN methods. The quality of the classification map of SSRN and HybridSN is far better than other methods. Among SSRN and HybridSN, the maps generated by HybridSN in the small segment are better than SSRN. Fig. 3 shows the confusion matrix for the HSI classification performance of the proposed $HybridSN$ over IP, UP, and SA data sets, respectively. The accuracy and loss convergence for 100 epochs of training and validation sets are portrayed in Fig. 4 for the proposed method. It can be seen that the convergence is achieved in approximately 50 epochs which points

out the fast convergence of our method. The computational efficiency of *HybridSN* model appears in term of training and testing times in Table III. The proposed model is more efficient than 3-D-CNN. The impact of spatial dimension over the performance of *HybridSN* model is reported in Table IV. It has been found that the used 25×25 spatial dimension is most suitable for the proposed method. We have also computed the results with even less training data, i.e., only 10% of total samples and have summarized the results in Table V. It is observed from this experiment that the performance of each model decreases slightly, whereas the proposed method is still able to outperform other methods in almost all cases.

IV. Conclusion

This letter has introduced a hybrid 3-D and 2-D model for HSI classification. The proposed HybridSN model basically combines the complementary information of spatio-spectral and spectral in the form of 3-D and 2-D convolutions, respectively. The experiments over three benchmark data sets compared with the recent state-of-the-art methods confirm the superiority of the proposed method. The proposed model is computationally efficient than the 3-D-CNN model. It also shows the superior performance for small training data.

References

[1] C.-I. Chang, *Hyperspectral Imaging: Techniques for Spectral Detection and Classification*, vol. 1. Springer Science & Business Media, 2003.

[2] G. Camps-Valls, D. Tuia, L. Bruzzone, and J. A. Benediktsson, "Advances in hyperspectral image classification: Earth monitoring with statistical learning methods," *IEEE Signal Process. Mag.*, vol. 31, no. 1, pp. 45–54, Jan. 2014.

[3] J. Yang and J. Qian, "Hyperspectral image classification via multiscale joint collaborative representation with locally adaptive dictionary," *IEEE Geosci. Remote Sens. Lett.*, vol. 15, no. 1, pp. 112–116, Jan. 2018.

[4] L. Fang, N. He, S. Li, A. J. Plaza, and J. Plaza, "A new spatial–spectral feature extraction method for hyperspectral images using local covariance matrix representation," *IEEE Trans. Geosci. Remote Sens.*, vol. 56, no. 6, pp. 3534–3546, Jun. 2018.

[5] G. Camps-Valls, L. Gomez-Chova, J. Munoz-Mari, J. Vila-Frances, and J. Calpe-Maravilla, "Composite kernels for hyperspectral image classification," *IEEE Geosci. Remote Sens. Lett.*, vol. 3, no. 1, pp. 93–97, Jan. 2006.

[6] J. Li, X. Huang, P. Gamba, J. M. Bioucas-Dias, L. Zhang, J. A. Benediktsson, and A. Plaza, "Multiple feature learning for hyperspectral image classification," *IEEE Trans. Geosci. Remote Sens.*, vol. 53, no. 3, pp. 1592–1606, Mar. 2015.

[7] Q. Gao, S. Lim, and X. Jia, "Hyperspectral image classification using joint sparse model and discontinuity preserving relaxation," *IEEE Geosci. Remote Sens. Lett.*, vol. 15, no. 1, pp. 78–82, Jan. 2018.

[8] P. Gao, J. Wang, H. Zhang, and Z. Li, "Boltzmann entropy-based unsupervised band selection for hyperspectral image classification," *IEEE Geosci. Remote Sens. Lett.*, vol. 16, no. 3, pp. 462–466, Mar. 2019.

[9] P. Hu, X. Liu, Y. Cai, and Z. Cai, "Band selection of hyperspectral images using multiobjective optimization-based sparse self-representation," *IEEE Geosci. Remote Sens. Lett.*, vol. 16, no. 3, pp. 452–456, Mar. 2019.

[10] B. Tu, X. Zhang, X. Kang, G. Zhang, J. Wang, and J. Wu, "Hyperspectral image classification via fusing correlation coefficient and joint sparse representation," *IEEE Geosci. Remote Sens. Lett.*, vol. 15, no. 3, pp. 340–344, Mar. 2018.

[11] T. Dundar and T. Ince, "Sparse representation-based hyperspectral image classification using multiscale superpixels and guided filter," *IEEE Geosci. Remote Sens. Lett.*, vol. 16, no. 2, pp. 246–250, Feb. 2019.

[12] A. Krizhevsky, I. Sutskever, and G. E. Hinton, "ImageNet classification with deep convolutional neural networks," in *Proc. Adv. Neural Inf. Process. Syst.*, 2012, pp. 1097–1105.

[13] K. He, X. Zhang, S. Ren, and J. Sun, "Deep residual learning for image recognition," in *Proc. IEEE Conf. Comput. Vis. Pattern Recognit.*, Jun. 2016, pp. 770–778.

[14] S. K. Roy, S. Manna, S. R. Dubey, and B. B. Chaudhuri, "LiSHT: Non-parametric linearly scaled hyperbolic tangent activation function for neural networks," 2019, *arXiv:1901.05894*. [Online]. Available: https://arxiv.org/abs/1901.05894

[15] S. Ren, K. He, R. Girshick, and J. Sun, "Faster R-CNN: Towards real-time object detection with region proposal networks," in *Proc. Adv. Neural Inf. Process. Syst.*, 2015, pp. 91–99.

[16] K. He, G. Gkioxari, P. Dollar, and R. Girshick, "Mask R-CNN," in *Proc. IEEE Int. Conf. Comput. Vis. (ICCV)*, Oct. 2017, pp. 2961–2969.

[17] S. H. S. Basha, S. Ghosh, K. K. Babu, S. R. Dubey, V. Pulabaigari, and S. Mukherjee, "RCCNet: An efficient convolutional neural network for histological routine colon cancer nuclei classification," in *Proc. 15th Int. Conf. Control, Autom., Robot., Vis. (ICARCV)*, Nov. 2018, pp. 1222–1227.

[18] V. K. Repala and S. R. Dubey, "Dual CNN models for unsupervised monocular depth estimation," 2018, *arXiv:1804.06324*. [Online]. Available: https://arxiv.org/abs/1804.06324

[19] C. Nagpal and S. R. Dubey, "A performance evaluation of convolutional neural networks for face anti spoofing," in *Proc. IEEE Int. Joint Conf. Neural Netw. (IJCNN)*, Mar. 2019, pp. 1–8.

[20] X. Kang, B. Zhuo, and P. Duan, "Dual-path network-based hyperspectral image classification," *IEEE Geosci. Remote Sens. Lett.*, vol. 16, no. 3, pp. 447–451, Mar. 2019.

[21] Y. Yu, Z. Gong, C. Wang, and P. Zhong, "An unsupervised convolutional feature fusion network for deep representation of remote sensing images," *IEEE Geosci. Remote Sens. Lett.*, vol. 15, no. 1, pp. 23–27, Jan. 2018.

[22] W. Li, C. Chen, M. Zhang, H. Li, and Q. Du, "Data augmentation for hyperspectral image classification with deep CNN," *IEEE Geosci. Remote Sens. Lett.*, vol. 16, no. 4, pp. 593–597, Apr. 2019.

[23] W. Song, S. Li, L. Fang, and T. Lu, "Hyperspectral image classification with deep feature fusion network," *IEEE Trans. Geosci. Remote Sens.*, vol. 56, no. 6, pp. 3173–3184, Jun. 2018.

[24] G. Cheng, Z. Li, J. Han, X. Yao, and L. Guo, "Exploring hierarchical convolutional features for hyperspectral image classification," *IEEE Trans. Geosci. Remote Sens.*, vol. 56, no. 11, pp. 6712–6722, Nov. 2018.

[25] J. M. Haut, S. Bernabé, M. E. Paoletti, R. Fernandez-Beltran, A. Plaza, and J. Plaza, "Low–high-power consumption architectures for deep-learning models applied to hyperspectral image classification," *IEEE Geosci. Remote Sens. Lett.*, vol. 16, no. 5, pp. 776–780, May 2019.

[26] Y. Chen, H. Jiang, C. Li, X. Jia, and P. Ghamisi, "Deep feature extraction and classification of hyperspectral images based on convolutional neural networks," *IEEE Trans. Geosci. Remote Sens.*, vol. 54, no. 10, pp. 6232–6251, Oct. 2016.

[27] Z. Zhong, J. Li, Z. Luo, and M. Chapman, "Spectral–spatial residual network for hyperspectral image classification: A 3-D deep learning framework," *IEEE Trans. Geosci. Remote Sens.*, vol. 56, no. 2, pp. 847–858, Feb. 2018.

[28] L. Mou, P. Ghamisi, and X. X. Zhu, "Unsupervised spectral–spatial feature learning via deep residual Conv–Deconv network for hyperspectral image classification," *IEEE Trans. Geosci. Remote Sens.*, vol. 56, no. 1, pp. 391–406, Jan. 2018.

[29] M. E. Paoletti, J. M. Haut, R. Fernandez-Beltran, J. Plaza, A. J. Plaza, and F. Pla, "Deep pyramidal residual networks for spectral–spatial hyperspectral image classification," *IEEE Trans. Geosci. Remote Sens.*, vol. 57, no. 2, pp. 740–754, Feb. 2019.

[30] M. E. Paoletti *et al.*, "Capsule networks for hyperspectral image classification," *IEEE Trans. Geosci. Remote Sens.*, vol. 57, no. 4, pp. 2145–2160, Apr. 2019.

[31] L. Fang, Z. Liu, and W. Song, "Deep hashing neural networks for hyperspectral image feature extraction," *IEEE Geosci. Remote Sens. Lett.*, to be published.

[32] S. Ji, W. Xu, M. Yang, and K. Yu, "3D convolutional neural networks for human action recognition," *IEEE Trans. Pattern Anal. Mach. Intell.*, vol. 35, no. 1, pp. 221–231, Jan. 2013.

[33] F. Melgani and L. Bruzzone, "Classification of hyperspectral remote sensing images with support vector machines," *IEEE Trans. Geosci. Remote Sens.*, vol. 42, no. 8, pp. 1778–1790, Aug. 2004.

[34] K. Makantasis, K. Karantzalos, A. Doulamis, and N. Doulamis, "Deep supervised learning for hyperspectral data classification through convolutional neural networks," in *Proc. IEEE Int. Geosci. Remote Sens. Symp. (IGARSS)*, Jul. 2015, pp. 4959–4962.

[35] A. B. Hamida, A. Benoit, P. Lambert, and C. B. Amar, "3-D deep learning approach for remote sensing image classification," *IEEE Trans. Geosci. Remote Sens.*, vol. 56, no. 8, pp. 4420–4434, Aug. 2018.

[36] M. He, B. Li, and H. Chen, "Multi-scale 3D deep convolutional neural network for hyperspectral image classification," in *Proc. IEEE Int. Conf. Image Process. (ICIP)*, Sep. 2017, pp. 3904–3908.